Angewandte Chemie
Eine Zeitschrift der Gesellschaft Deutscher Chemiker

Supporting Information

Persistent *peri*-Heptacene: Synthesis and In Situ Characterization

M. R. Ajayakumar, Ji Ma, Andrea Lucotti, Karl Sebastian Schellhammer, Gianluca Serra, Evgenia Dmitrieva, Marco Rosenkranz, Hartmut Komber, Junzhi Liu, Frank Ortmann, Matteo Tommasini, and Xinliang Feng**

anie_202102757_sm_miscellaneous_information.pdf

Supporting Information

Table of Contents

1. Experimental details

General methods and materials: All the starting materials were obtained from Sigma Aldrich, TCI, abcr, or chempur and the catalysts were sourced from Strem. All these chemicals were used as received. Thin layer chromatography (TLC) was carried out on aluminium plates coated with silica gel mixed with fluorescent indicator and was sourced from Merck, Germany.

NMR spectra were recorded on a Bruker Avance III 300 and on a Bruker Avance III 500 spectrometer using CD_2Cl_2 ($\delta(^1H)$ = 5.32 ppm; $\delta(^{13}C)$ = 53.7 ppm) or $C_2D_2Cl_4$ ($\delta(^1H)$ = 5.98 ppm; $\delta(^{13}C)$ = 73.7 ppm) as solvent, lock and internal standard. The 1D and 2D NMR spectra were recorded using the standard pulse programs included in the Bruker Topspin 3.2 software package. Coupling constants (*J* values) are given in Hz whereas chemical shifts are reported in parts per million (ppm). Splitting patterns are designated as s (singlet), d (doublet), t (triplet), q (quartet), and m (multiplets).

The high resolution mass spectrometry analyses were performed by using Bruker Autoflex MALDI TOF (DCTB or dithranol as the matrix) and Agilent Q-TOF (APCI mode using acetonitrile as solvent) instruments. UV-vis-NIR spectra were measured on an Agilent Cary 5000 spectrophotometer by using 10 mm optical-path quartz cell at room temperature.

High-Resolution Atmospheric Pressure Chemical Ionization (APCI) mass spectra were recorded with Agilent 6538 Ultra High Definition (UHD) Accurate-Mass Q-TOF LC/MC system, using the positive mode.

2. Synthesis

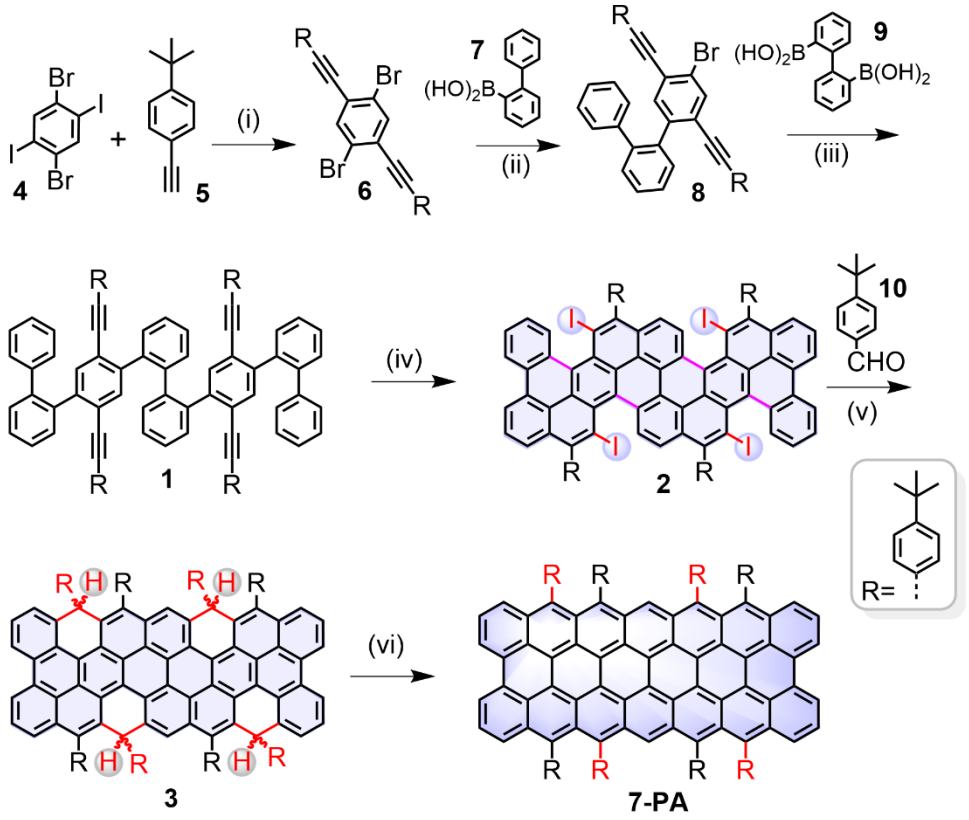

Scheme S1: Synthesis of *peri*-heptacene (**7-PA**). Reagents and conditions: (i) $Pd(PPh_3)_2Cl_2$, CuI, Et_3N, THF, RT, 24 h, 87%; (ii) $Pd(PPh_3)_4$, K_2CO_3, toluene/EtOH/H_2O, 85 °C, 24 h, 50%; (iii) $Pd(PPh_3)_4$, K_2CO_3, toluene/EtOH/H_2O, 85 °C, 24 h, 41%; (iv) ICl, dichloromethane, −78 °C, 3 h, 29%; (v) (1) n-BuLi, 4-(*tert*-butyl)benzaldehyde (**10**), toluene, −10 °C, 2 h; (2) $BF_3{\cdot}OEt_2$, dichloromethane, 25 °C, 30 min, 40% (over two steps); (vi) DDQ, toluene, 25 °C, 10 min.

Compound **6** [1a] and biphenyl-2,2'-diboronic acid **9** [1b] are synthesized as reported.

Synthesis of 4-bromo-2,5-bis((4-*tert*-butylphenyl)ethynyl)-1,1':2',1''-terphenyl (8)

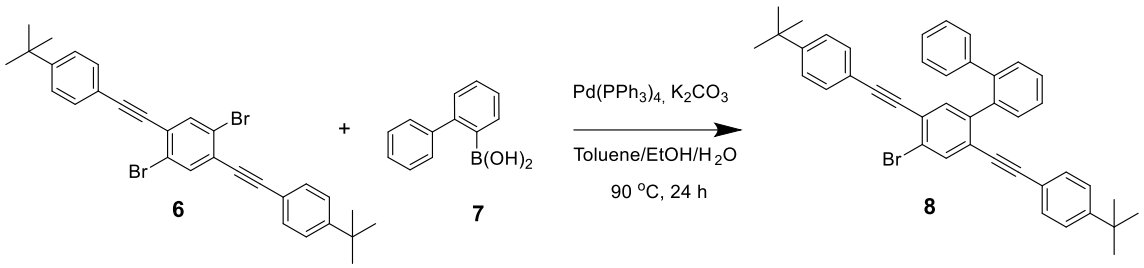

A flask was charged with **6** (5.3 g, 9.7 mmol), biphenyl-2-boronic acid **7** (1.9 g, 9.7 mmol), and K_2CO_3 (21.5 g, 155.2 mmol) along with toluene (120 mL), ethanol (33 mL) and water (45 mL). The mixture was degassed by Ar bubbling for 30 min and then $Pd(PPh_3)_4$ (896.9 mg, 0.78 mmol) was added. The solution was bubbled with Ar for 10 min and heated at 90 °C for 24 h under Ar. The reaction mixture was allowed to reach room temperature and the organic layer was separated. The aqueous phase was extracted with 50 mL of dichloromethane (DCM) and the combined organic layers were dried over $MgSO_4$. The solvent was removed under reduced pressure and the residue was purified by column chromatography on silica (*iso*-hexane:DCM = 3:1) to afford **8** as white solid (3 g, 50%). R_f = 0.44 (*iso*-hexane/DCM 3:1 *v/v*). ^{1}H NMR (300 MHz, CD_2Cl_2): δ 7.69 (s, 1H), 7.50 - 7.37 (m, 8H), 7.31 (m, 2H), 7.19 (m, 6H), 7.11 (m, 2H), 1.32 (s, 9H), 1.29 (s, 9H). ^{13}C NMR (75 MHz, CD_2Cl_2): δ 152.48, 152.15, 143.51, 141.42, 140.99, 137.73, 134.88, 134.56, 131.32, 131.10, 130.72, 130.04, 129.59, 128.33, 127.77, 126.94, 126.65, 125.53, 125.40, 124.58, 123.25, 119.54, 119.47, 95.49, 95.34, 87.25, 86.98, 34.77, 30.84. HR-MS APCI (m/z): calcd for $C_{42}H_{37}Br$ $[M]^+$, 620.2079; found, 620.2074.

Synthesis of 1

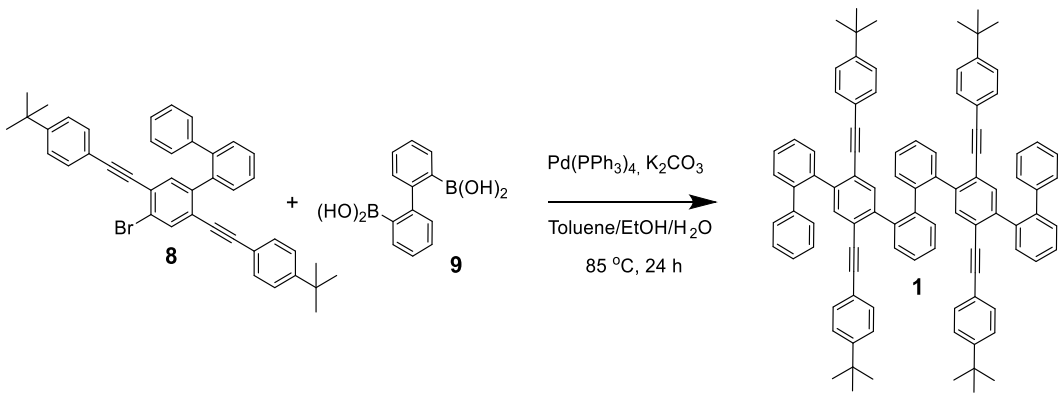

A flask was charged with **8** (1.2 g, 2.0 mmol), biphenyl-2,2'-diboronic acid **9** (190.0 mg, 0.79 mmol), and K_2CO_3 (1.3 g, 9.4 mmol) along with toluene (32 mL), ethanol (8 mL) and water (8 mL). The mixture was degassed by Ar bubbling for 30 min and then $Pd(PPh_3)_4$ (90.8 mg, 0.08 mmol) was added. The solution was bubbled with Ar for 10 min and heated at 85 °C for 24 h under Ar. The reaction mixture was allowed to reach room temperature and the organic layer was separated. The aqueous phase was extracted with DCM (50 mL) and the combined organic layers were dried over $MgSO_4$. The solvent was removed under reduced pressure and the residue was purified by column chromatography on silica (*iso*-hexane:DCM = 4:1) to afford **1** as off-white solid (400 mg, 41%). R_f = 0.49 (*iso*-hexane/DCM 2:1 *v/v*). ^{1}H NMR (300 MHz, CD_2Cl_2): δ 7.85 – 6.60 (46H), 1.27 (s, 36H). ^{13}C NMR (75 MHz, CD_2Cl_2): δ 130.95, 129.61, 127.61, 126.35, 125.25, 125.18, 112.96, 34.60, 30.86. HR-MS MALDI (m/z): calcd for $C_{96}H_{82}$ $[M]^+$, 1234.6417; found, 1234.6416 (matrix: dithranol).

Synthesis of 2

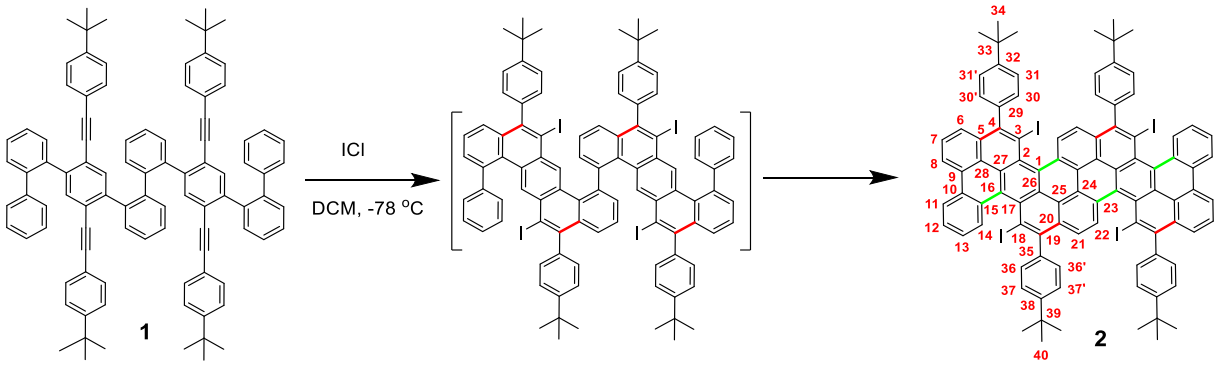

1 (240 mg, 0.19 mmol) was dissolved in 25 mL of anhydrous DCM and cooled down to –78 °C. To this stirring solution, 2 mL of ICl (200 mg, 1.2 mmol) solution in DCM was added dropwise using a syringe over 5 min. The mixture was kept at –78 °C for 1.5 h and then quenched by adding saturated aqueous Na_2SO_3 solution (5 mL). This solution was mixed with 50 mL water and extracted with 2 × 50 mL of DCM. The organic layer was dried over $MgSO_4$ and the solvent was removed under reduced pressure. The obtained crude solid was purified by column chromatography on silica (*iso*-hexane:DCM = 3:1) to afford **2** as deep blue solid (100 mg, 29%). R_f = 0.34 (*iso*-hexane/DCM 3:1 *v/v*). ^{1}H NMR (500 MHz, $C_2D_2Cl_4$): δ 9.16 (d, 8.7 Hz, 2H; 22), 9.16 (d, 8.0 Hz, 2H; 8), 8.87 (d, 8.3 Hz, 2H; 11), 8,74

(d, 8.3 Hz, 2H; 14), 8.40 (d, 8.7 Hz, 2H; 21), 8.06 (t, 8.0 Hz, 2H; 7), 7.94 (d, 8.0 Hz, 2H; 6), 7.91 (dd, 2H; 30), 7.89 (dd, 2H; 36), 7.85-7.70 (8H; 12, 31, 37, 37‘), 6.68 (t, 7.5 Hz, 2H; 13), 7.54 (dd, 2H; 31‘), 7.45 (dd, 2H; 36‘), 7.08 (dd, 2H; 30‘), 1.54 (s, 18H; 40), 1.50 (s, 18H; 34). ^{13}C NMR (125 MHz, $C_2D_2Cl_4$): δ 151.0 (38), 150.9 (32), 148.3 (4),147.6 (19), 142.4 (29), 142.1 (35), 134.3 (14), 133.3 (22), 132.3 (5), 131.1 (36), 130.4 (36‘), 130.2 (30), 130.1 (30’), 129.9 (n. a.), 129.7 (9), 128.9 (10), 128.5 (15), 128.1 (16), 128.0 (6), 127.5 (12, 2 x n. a.), 127.4 (23 or 25), 126.9 (7), 126.2 (13 and 21), 125.3 (31’, 37, 37’), 124.8 (n. a.), 124.7 (31), 124.6 (n. a.), 122.6 (n. a.), 122.3 (8, 28), 120.9 (23 or 25), 100.8 and 100.3 (3, 18), 34.6 (33, 39), 31.4 (34, 40). *Note*: The 4-*tert* butyl phenyl groups are slowly rotating on the NMR time scale. The positions 30’ and 36’ are defined by their weak ROESY correlations to H_6 and H_{21}, respectively. In the ^{1}H NMR spectrum, all eight phenyl signals are doublet of doublets (dd) with $^3J_{HH}$ ~ 8.2 Hz and $^4J_{HH}$ ~ 2.0 Hz. Furthermore, several ^{13}C NMR signals could not be assigned (n. a.) due to missing HMBC correlations. HR-MS MALDI (m/z): calcd for $C_{96}H_{70}I_4$ $[M]^+$, 1730.1656; found, 1730.1730 (matrix: dithranol).

Synthesis of 3

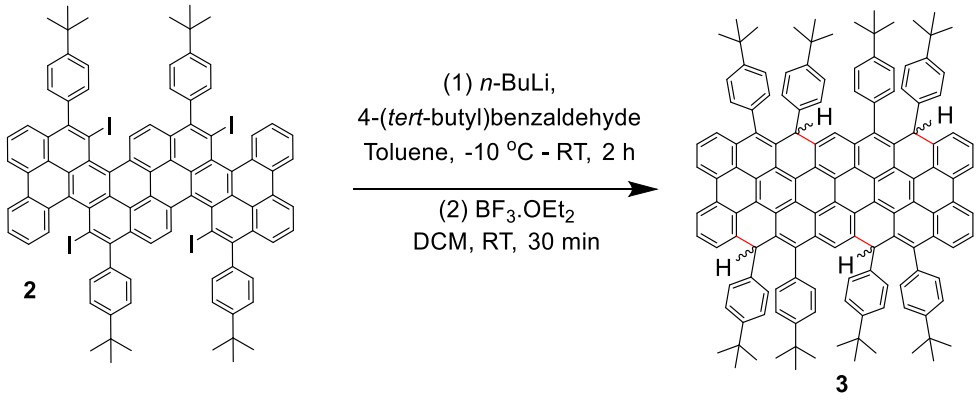

Compound **2** (20 mg, 0.011 mmol) was dissolved in anhydrous toluene (4 mL) and brought to -10 °C on an ice-salt bath. To this solution, 1.6 M n-BuLi (50 µL, 0.069 mmol) in hexane was slowly injected. After stirring for 10 min, 4-(*tert*-butyl)benzaldehyde (**10**) in toluene (7 equiv.) was injected dropwise. With stirring, the solution was gradually warmed to RT over a time period of 3 h and the reaction was quenched with MeOH. The reaction mixture was mixed with EtOAc (30 mL) and the organic phase was washed with water. After drying over $MgSO_4$, the organic solvent was evaporated under reduced pressure to afford viscous yellow

oil. This was redissolved in anhydrous DCM (10 mL) and mixed with BF_3•OEt_2 (0.40 mL, 2.24 mmol). After 30 min stirring, the reaction was quenched with MeOH. The solution was diluted with DCM and washed with water. The organic layer was separated, dried over $MgSO_4$ and evaporated in vacuo. The residue was mixed with MeOH and the solid obtained was washed with MeOH. The obtained residue was purified by flash silica column chromatography with *iso*-hexane/DCM (2:1) as eluent to afford the configurational isomers of **10** (8 mg, 40%) as purple coloured solid. R_f = 0.5 (*iso*-hexane/DCM = 2:1 *v/v*). The structural characterization of **3** with NMR spectroscopy is not possible due to the presence of a mixture of non-isolable stereoisomers resulting in a very complex ^{1}H NMR spectrum (Figure S20). HR-MS MALDI (m/z): calcd for $C_{140}H_{122}$ $[M]^+$, 1802.9547; found, 1802.9496 (matrix: dithranol). FT-IR (powder, ATR): 3056, 3025, 2955, 2904, 2866, 1601, 1510, 1476, 1458, 1392, 1358, 1261, 1108, 1019, 883, 821, 755 cm^{-1}; FT-RAMAN (film): 1610, 1598, 1575, 1531, 1482, 1429, 1397, 1334, 1315, 1288, 1197 $cm^{-1.}$

Synthesis of 7-PA

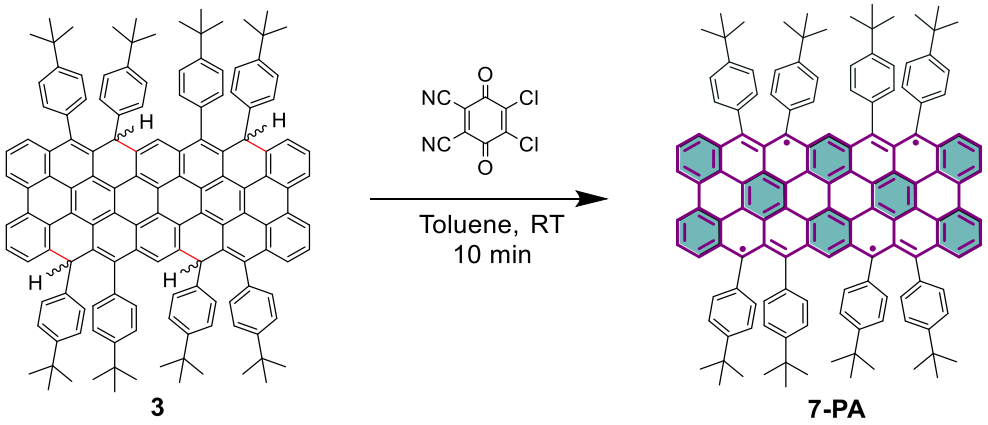

A solution of precursor **3** (5 mg, 2.7 µmol) in anhydrous and Ar bubbled toluene (2 mL) was mixed with DDQ (1.57 mg, 6.9 µmol) under Ar at RT. Upon occasionally shaking by hand with 10 min, the bright purple coloured solution then turned to a dark brown solution, indicating the *in-situ* generation of the **7-PA**. Further efforts to purify **7-PA** are not successful due to the decomposition even under inert conditions. HR-MS MALDI (m/z): calcd for $C_{140}H_{118}$ $[M]^+$, 1798.9234; found, 1798.9257 (matrix: dithranol). FT-RAMAN (film): 1593, 1563, 1520, 1493, 1405, 1378, 1332, 1297, 1269, 1246, 1200 cm^{-1}.

3. FT-Raman spectroscopy

Raman measurements: The FT-Raman spectra were recorded with a resolution of 4 cm^{-1} using the Nicolet NXR9650 instrument equipped with an InGaAs detector and a Nd-YVO_4 laser providing the 1064 nm excitation line. The spectra were recorded in backscattering geometry with a laser spot diameter of approximately 50 μm. For precursor **3** the power at the sample was approximately 0.8 W (128 scans were accumulated for a total measurement time of about 5 min). For **7-PA** the power at the sample was approximately 0.7 W (16 scans were accumulated for a total measurement time of about 30 s). For DDQ the power at the sample was approximately 0.9 W (128 scans were accumulated for a total measurement time of about 5 min).

Preparation of samples for Raman spectroscopy: The sample of precursor **3** was prepared as a film cast on metal (brass) from toluene solution (1 mM). The good thermal conductivity of the metal surface allows to overcome the laser-induced heating of the sample which otherwise hinders the reliable collection of the FT-Raman spectrum. The **7-PA** sample was obtained from the precursor **3** film on metal upon dropping 50 microliters of a toluene solution of DDQ (2 mM). The reaction occurs in the film, as evidenced by a quick color change. The **7-PA** film was measured in the same experimental conditions as the precursor **3** film, after complete solvent evaporation (which occurs within a few seconds). The reference FT-Raman spectrum of DDQ was measured on powders.

Computational details: Density functional theory (DFT) calculations of the Raman spectra were carried out in gas phase on the complete molecular structures of **7-PA** and precursor **3**. We adopted the CAM-B3LYP functional [2] and the 6-311G(d,p) basis set [3]. In the case of **7-PA**, to account for the open shell nature of the system, we adopted the unrestricted scheme (UCAM-B3LYP/6-311G(d,p) – broken symmetry, singlet state). The vibrational frequencies and Raman activities of the two compounds (**3**, **7-PA**) were calculated using the Gaussian code [4]. The Raman spectra were simulated by weighted sums of normalized Lorentzian functions (unitary area; FWHM = 10 cm^{-1}); the weights of the Lorentzian functions have been fixed at the values of the computed Raman activities (units of $Å^4$/amu). Since DFT is known to overestimate vibrational frequencies, scale factors were applied that provide best linear fits between a selection of observed and computed Raman wavenumbers (see Table S1 for the list of the Raman features selected for this procedure). This least-square fitting yields scale factor values of 0.987 for **7-PA** and 0.966 for precursor **3**.

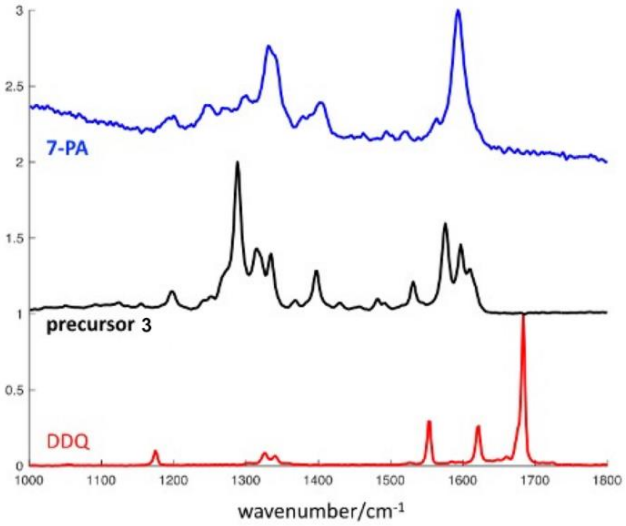

Figure S1: Experimental FT-Raman spectra of DDQ, precursor **3**, and **7-PA**. See Methods for the experimental details.

7-PA	expt. wavenumber (cm^{-1})	scaled wavenumber (cm^{-1})
D_1	1331	1298
D_1	1331	1301
D_2	1402	1428
G_a	1523	1531
G_b	1564	1558
G	1593	1604
precursor **3**	expt. wavenumber (cm^{-1})	scaled wavenumber (cm^{-1})
D	1288	1272
G_1	1576	1598
G_2	1597	1622

Table S1: Vibrational assignment of the Raman features of **7-PA** and precursor **3** (see Methods for details about the scaling of computed wavenumbers).

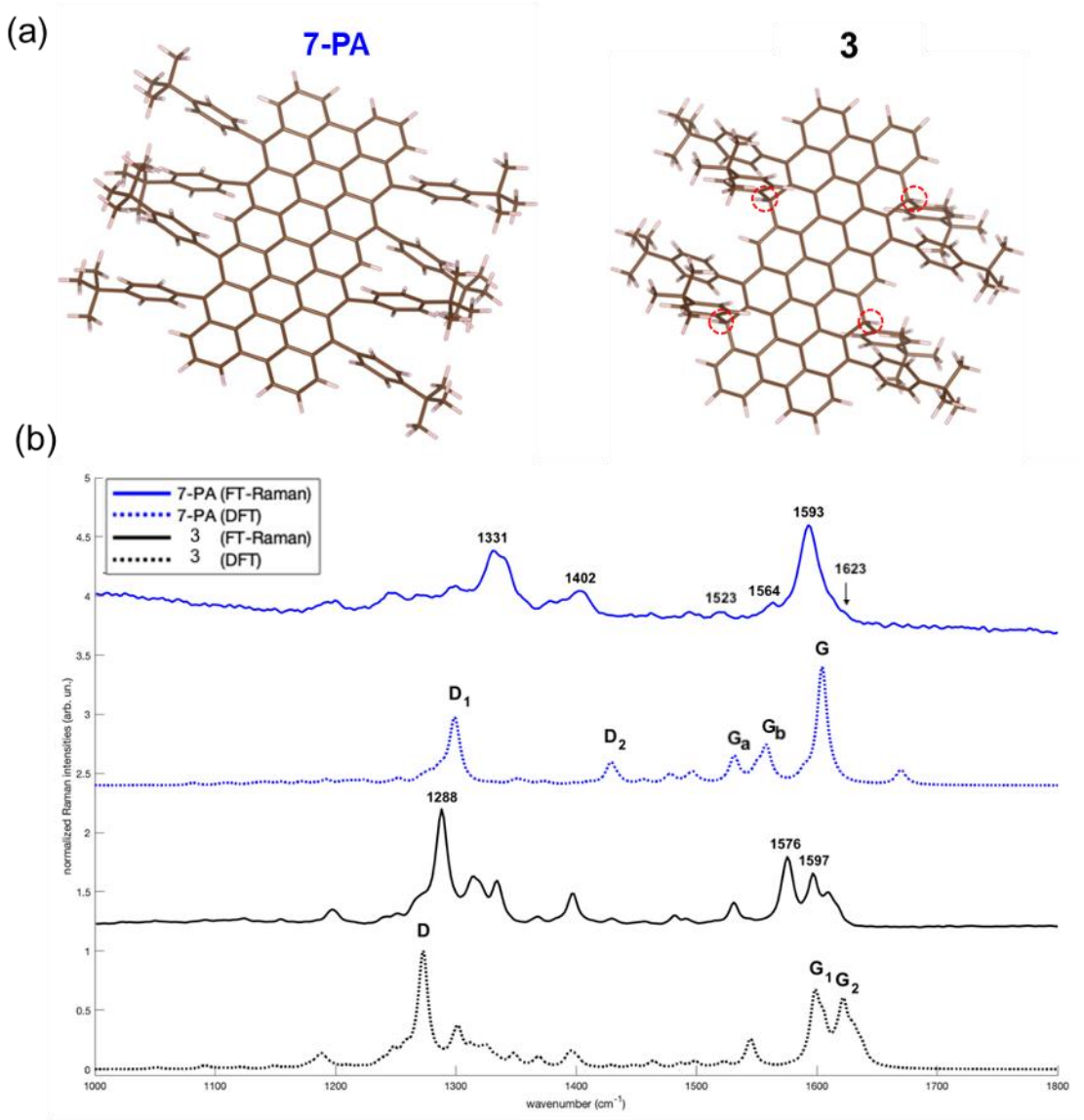

Figure S2: (a) Representation of the optimized molecular structures of **7-PA** and precursor **3**, as obtained from CAM-B3LYP/6-311G(d,p) DFT calculations. (b) Experimental (solid lines) and simulated (dashed lines) Raman spectra of **7-PA** (blue) and precursor **3** (black). Numerical labels indicate the wavenumbers (cm^{-1}) of the experimental peaks assigned to the computed G and D modes that are labelled following the notation of Table S1. See the Computational Details for information about the wavenumber scaling procedure.

The effects of intermolecular interactions in solid state. Even though the qualitative agreement between the computed Raman spectrum of **7-PA** and its experimental counterpart is satisfactory, a closer inspection (Figure S3) reveals a few discrepancies, namely: (i) two satellite peaks at lower wavenumber than the G line (G_a: 1531 cm^{-1}, G_b: 1558 cm^{-1}) are evident in the simulated spectrum, and not so much in the experiment; (ii) the positions of the

G and D_2 lines are shifted to higher wavenumber than the experiment, whereas the position of the D_1 line is shifted to lower wavenumber than the experiment; (iii) the peak assigned to the ring stretching of the lateral substituents of **7-PA** shows up at a too high-wavenumber (1670 cm^{-1}), whereas in the experiment is a weak shoulder in the high wavenumber side of the G band (1623 cm^{-1}).

By zooming the vertical scale in the experimental Raman spectrum of **7-PA**, we find that the computed bands mentioned at point (i) above (G_a, G_b) actually match two weak experimental features (Figure S3). The nuclear displacements of the G_a mode are described as a collective ring stretching, similar to the G mode of **7-PA**, but with an alternated phase along the different vibrating rings (see supplementary AVI file for details). The inspection of the G_b mode shows ring stretching patterns occurring along the other degenerate G mode of graphene, different from the displacement pattern observed for the G and G_a modes of **7-PA** (see ref. [5] and the supplementary AVI file for details).

A reasonable explanation for the other observed discrepancies (ii, iii) is due to the use of DFT models in the gas phase for simulating the Raman scattering of a sample in condensed phase. Of course, such models lack intermolecular interactions and crystal packing effects that may alter the planar shape of the molecule and the conformation of its substituents. Unfortunately, due to the large size of **7-PA**, testing DFT models of interacting dimers is prohibitive. Hence, we decided to verify the effects of distorting the structure of 7-PA along a low-wavenumber twisting mode (25 cm^{-1}; the mode is represented in the supplementary AVI file). This mode can describe a possible deviation from planarity that may be activated with minimal energy cost (due to the very low wavenumber). The Hessian of the distorted (twisted) **7-PA** structure has no negative eigenvalues, so this structure can be accepted for vibrational analysis. We compare in Figure S3 the Raman spectrum of the twisted **7-PA** model, and the spectrum computed for the nearly planar equilibrium structure, with the experimental spectrum. As expected, all principal Raman features of **7-PA** are affected by the twisting of the molecular structure. Only for the D_1 peak observed at 1331 cm^{-1}, the effect of twisting goes against the experimental observation (*i.e.*, D_1 red-shifts instead of blue-shifting). This result is due to the currently unknown molecular conformation of **7-PA** in the solid-state: the selected twisted geometry is not guaranteed to mimic the molecular distortion really taking place in the sample, which could also involve the distortion along other low-wavenumber modes.

Moreover, along the twisting mode also the conformation of the lateral substituents is affected: as a consequence, also the ring stretching modes shift significantly to lower wavenumber (from 1670 cm^{-1} to 1654 cm^{-1}).

In conclusion, we expect that by a proper consideration of the structure changes induced by intermolecular interactions (which would require additional information, *e.g.*, from X-ray diffraction) one may substantially improve the quality of the simulated Raman spectra.

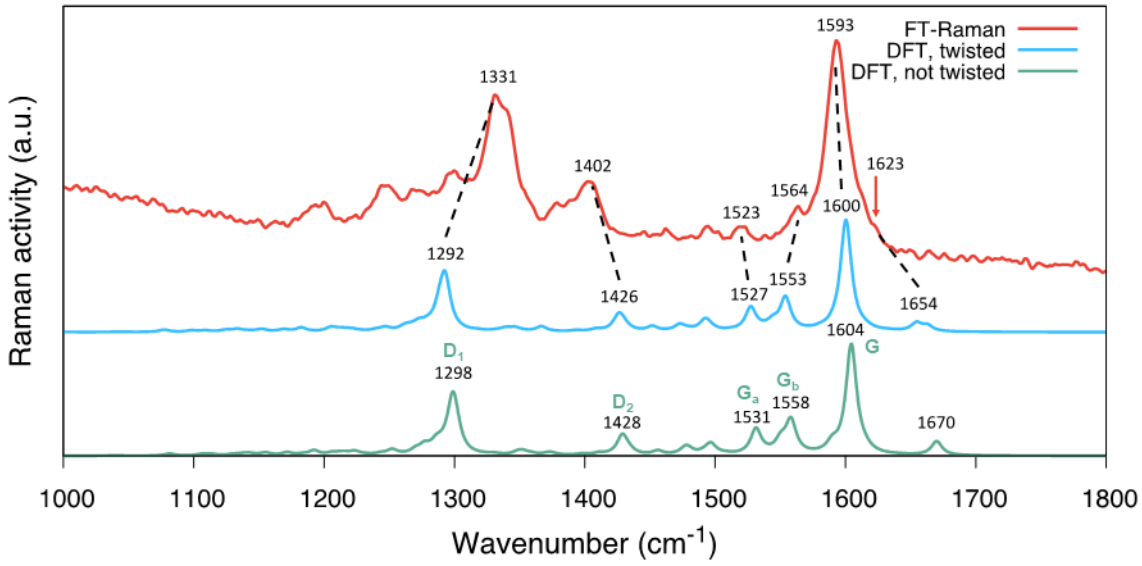

Figure S3: Experimental (red line) and simulated (light blue, green lines) Raman spectra of **7-PA**. DFT calculations have been carried out at the CAM-B3LYP/6-311G(d,p) level. The numerical labels indicate the wavenumbers (cm^{-1}) of peaks assigned to the computed G and D modes that are labelled following the notation of Table S1 (see the Computational Details for information about the wavenumber scaling procedure). The simulated Raman spectrum shown in light blue was obtained by displacing the equilibrium structure of **7-PA** along the twisting mode computed at 25 cm^{-1} (unscaled).

4. ESR Spectroscopy

EPR measurements were performed using a CW X-band EMXplus spectrometer with a premiumX microwave bridge (Bruker Biospin GmbH, Germany) and a high sensitivity resonator (ER 4119 HS, Bruker). The ESR spectra were recorded at 100 kHz modulation and at room temperature. For spectroelectrochemical experiments, the EPR spectrometer was linked to a HEKA potentiostat PG 390 (HEKA Elektronik, Germany) and a flat cell was

used. A platinum mesh as the working electrode, a silver chloride coated silver wire as the reference electrode, and a platinum wire as the counter electrode were used.

The *g* value (2.003) of **7-PA** is comparable to that of the **4-PA** and indicates that the spin density of **7-PA** is delocalized over the zigzag peripheries. With the *in-situ* generation of **7-PA**, the formation of DDQ monoradical anions ($DDQ^{\bullet-}$) is also observed (*g* = 2.0052 and linewidth = 0.2 G) (Figure S4-S6). Unfortunately, **7-PA** could not be isolated due to its high reactivity. Therefore, the detailed analysis of **7-PA** signal was not possible because of its superimposition with the strong EPR signal from $DDQ^{\bullet-}$ impurities.

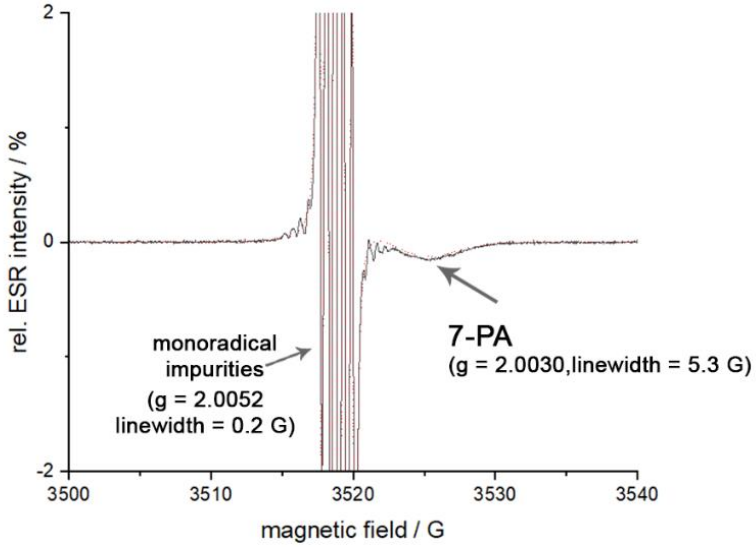

Figure S4: ESR spectrum of **7-PA** (8×10^{-4} M) in toluene recorded at RT. The **7-PA** was *in-situ* generated by mixing toluene solution of **3** with 2 equiv. DDQ. The monoradicals are identified as DDQ radical anions ($DDQ^{\bullet-}$), which are generated due to the side reactions of **7-PA** and DDQ (see controlled experiment for *in-situ* generated **4-PA** in Figure S5 and the electrochemically generated $DDQ^{\bullet-}$ in Figure S6), but the mechanism is unclear.

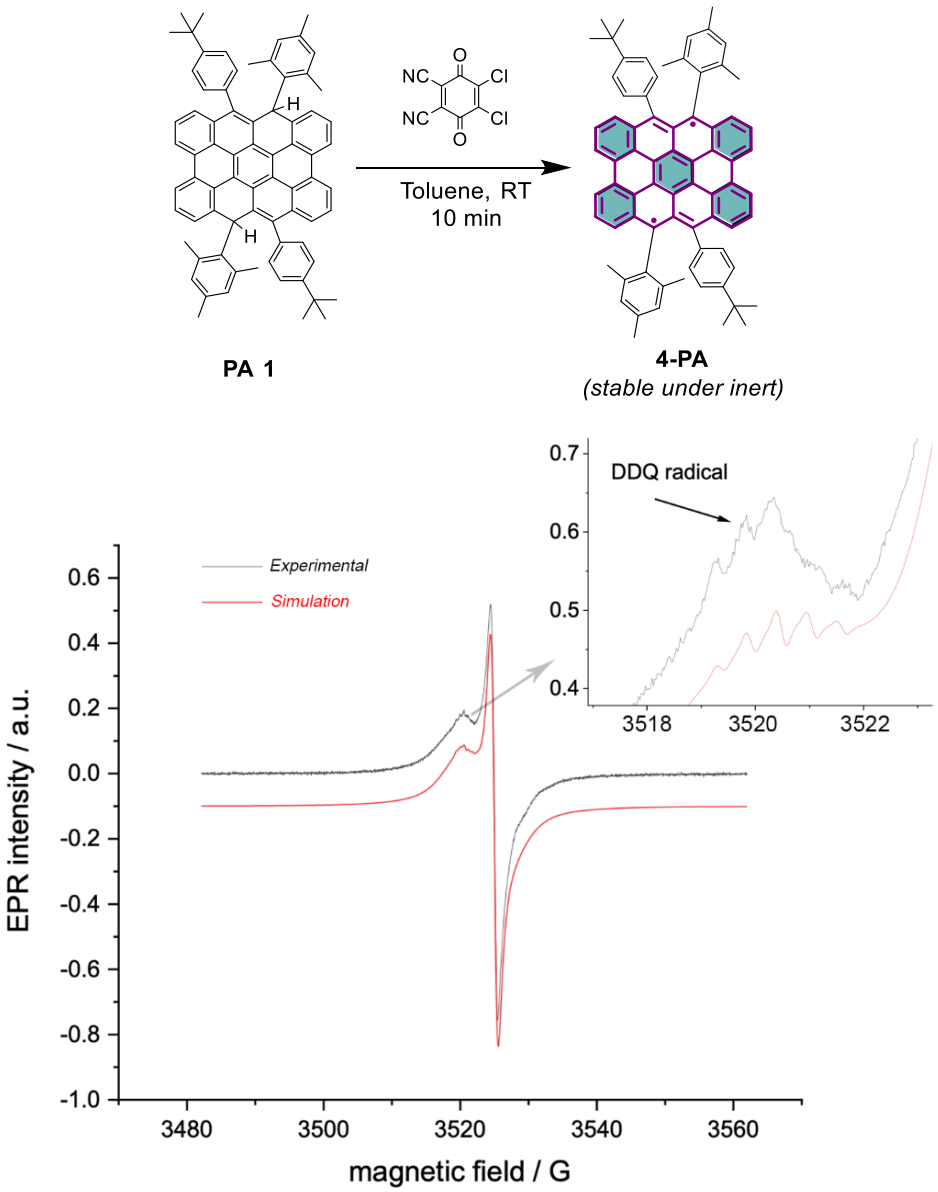

Figure S5: ESR spectrum of **4-PA** (1×10^{-3} M) in toluene recorded at RT. The **4-PA** was *in-situ* generated by mixing toluene solution of **PA 1** with 1 equiv. DDQ. The presence of $DDQ^{\bullet-}$ are confirmed by observing a quintet with g value of 2.0051 (linewidth = 0.2 G). To further confirm the existence of $DDQ^{\bullet-}$, we also carried out the electrochemical generation of $DDQ^{\bullet-}$ (see Figure S6).

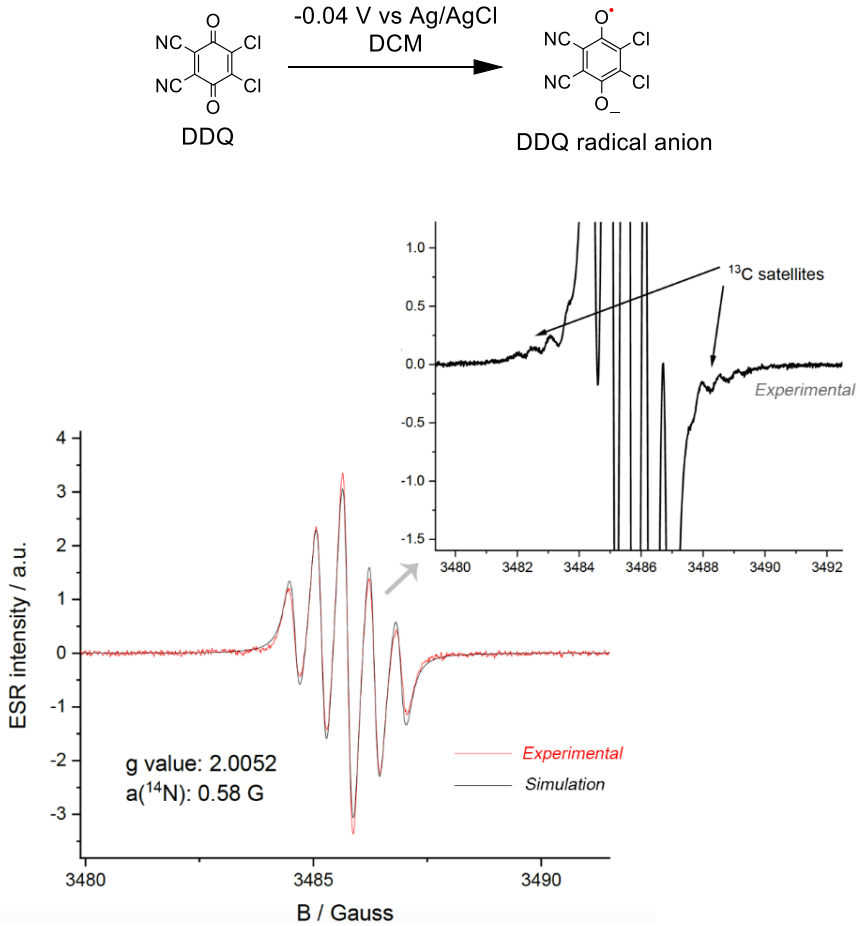

Figure S6: ESR spectrum of DDQ$^{\bullet-}$ (1×10^{-3} M) in DCM recorded at RT. The DDQ$^{\bullet-}$ was electrochemically generated by applying a have-wave potential of -0.04 V vs Ag/AgCl. The ESR spectrum of DDQ$^{\bullet-}$ exhibits a signal with g-value of 2.0052 and hyperfine coupling constants of 0.58 G due to two equivalent ^{14}N nuclei. The simulated and experimental spectra are in excellent agreement. The presence of DDQ$^{\bullet-}$ impurities in the *in-situ* generation of **7-PA** is thus confirmed, since those signals are similar with the electrochemically generated DDQ$^{\bullet-}$.

5. Open-shell simulations

Density functional theory (DFT) simulations were performed within the Gaussian09 software package to evaluate the open-shell characteristics [4]. According to the simulation of the vibrational spectra, the UCAM-B3LYP/6-311G(d,p) level of theory was used for geometry optimization. CASSCF(8,8)/6-31G** is used to calculate the diradical character y_0 and the tetraradical character y_1 based on the occupation numbers of the lowest unoccupied natural orbitals (LUNO and LUNO+1) [6].

This computational scheme is applied to systematically analyze the open-shell characteristics of the class of n-*peri*-acenes (n-PAs) from n = 2 to n=7. In addition, the singlet-triplet energy gap $\Delta E_{S\text{-}T}$ was evaluated at the UCAM-B3LYP/6-311G(d,p) level of theory as

$$\Delta E_{S\text{-}T} = \Delta E_T(q_T) - \Delta E_S(q_S),$$

where $\Delta E_S(q_S)$ and $\Delta E_T(q_T)$ are the total energies of the singlet diradical (open-shell) and triplet ground state, respectively, *i.e.*, $\Delta E_{S\text{-}T}$ denotes the minimum-to-minimum energy difference.

The behavior of the diradical character y_0, the tetraradical character y_1 and $\Delta E_{S\text{-}T}$ is depicted in Figure S6. The diradical character increases with extending the length of the molecule with **6-PA** and **7-PA** showing a complete diradical ground state. These molecules also exhibit a substantial tetraradical character. The unpaired electron density is obtained using Multiwfn [7]. It is depicted for the series of n-PAs in Figure S7. It is widely restricted to the zigzag periphery. Surprisingly, $\Delta E_{S\text{-}T}$ shows a minimum for **5-PA** and starts to increase again for longer molecules. It should be noted that these values are based on simulations of single molecules in gasphase and that the accuracy of density functional theory suffers from spin contamination by higher spin states [8,9]. Environmental effects and shortcomings of the level of theory used might also lead to the relatively large mismatch between simulated and experimentally measured singlet-triplet gap $\Delta E_{S\text{-}T}$ of **7-PA** and motivate extended theoretical analysis using multireference methods.

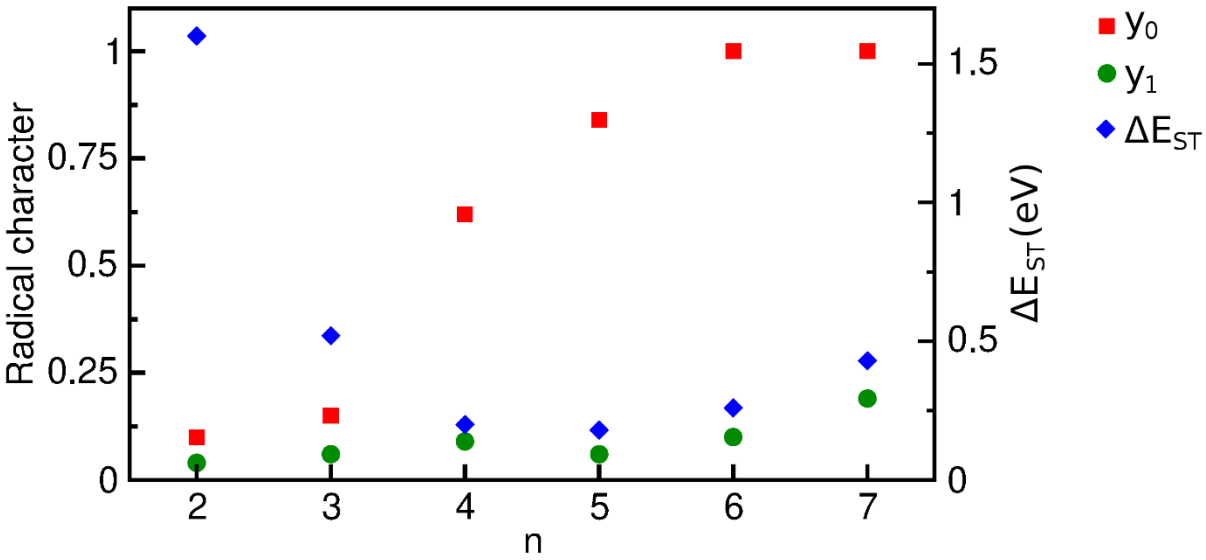

Figure S7: Open-shell characteristics of n-PAs.

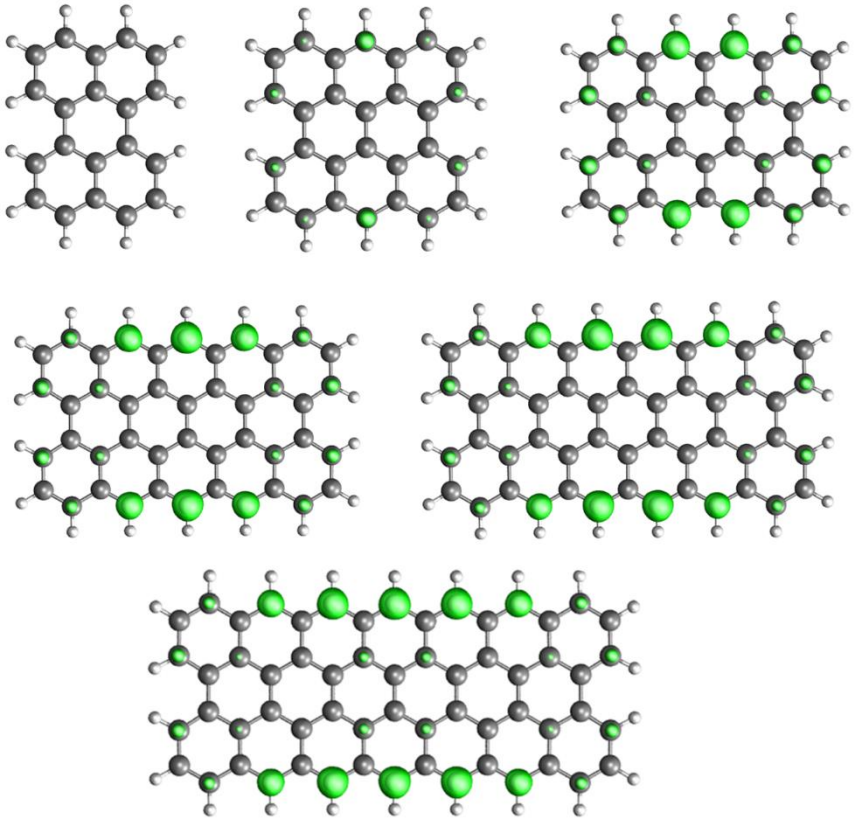

Figure S8: Density of unpaired electrons of n-PAs.

6. HR MALDI-TOF mass spectra

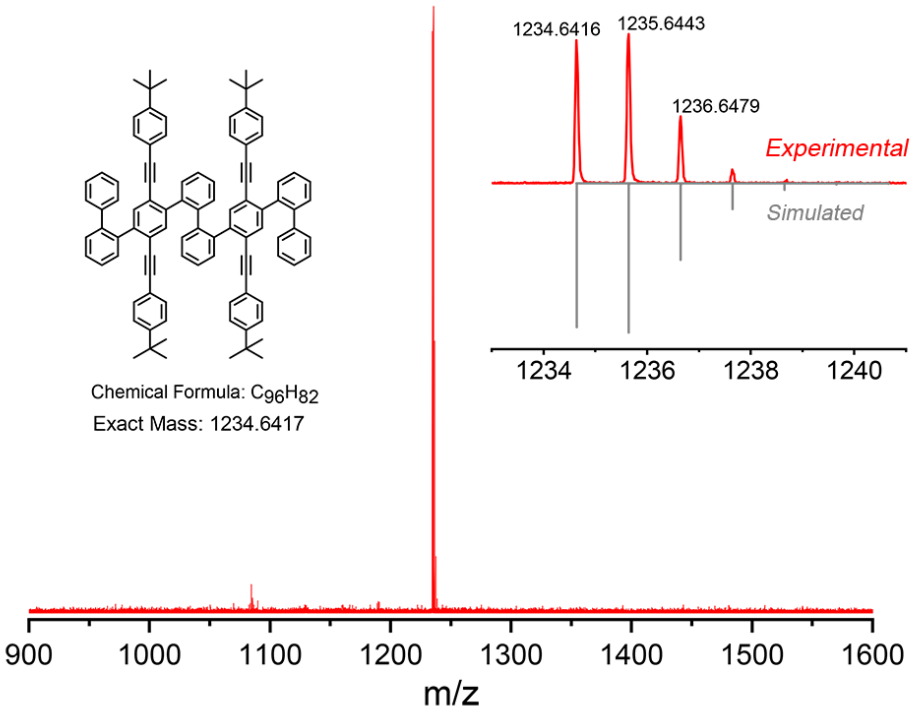

Figure S9: HR MALDI-TOF spectrum of **1** in DCTB.

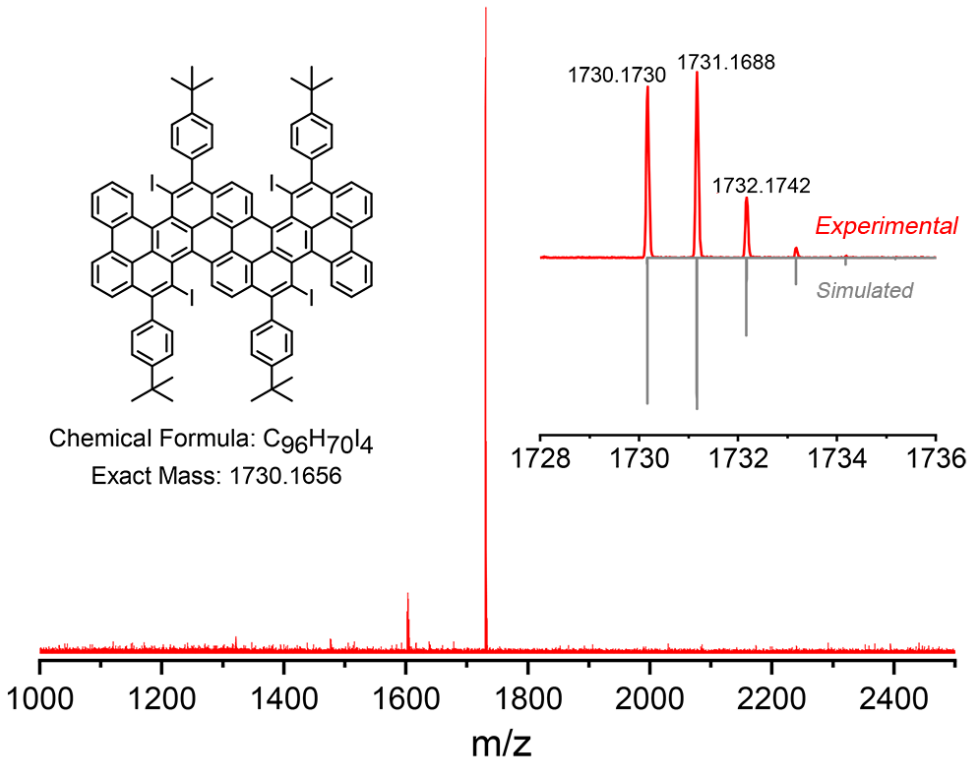

Figure S10: HR MALDI-TOF spectrum of **2** in dithranol.

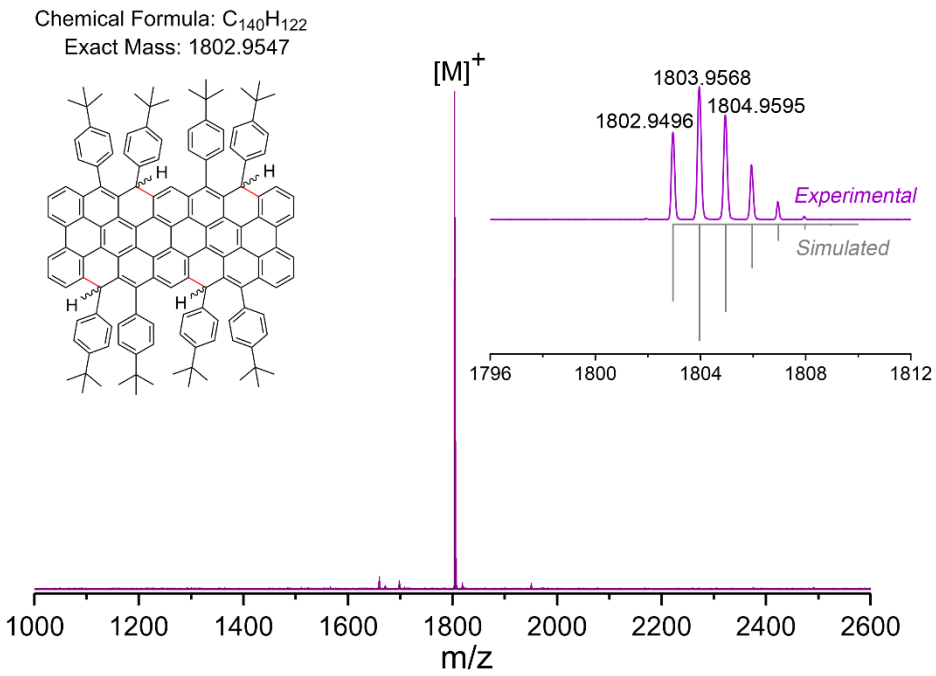

Figure S11: HR MALDI-TOF spectrum of **3** in dithranol.

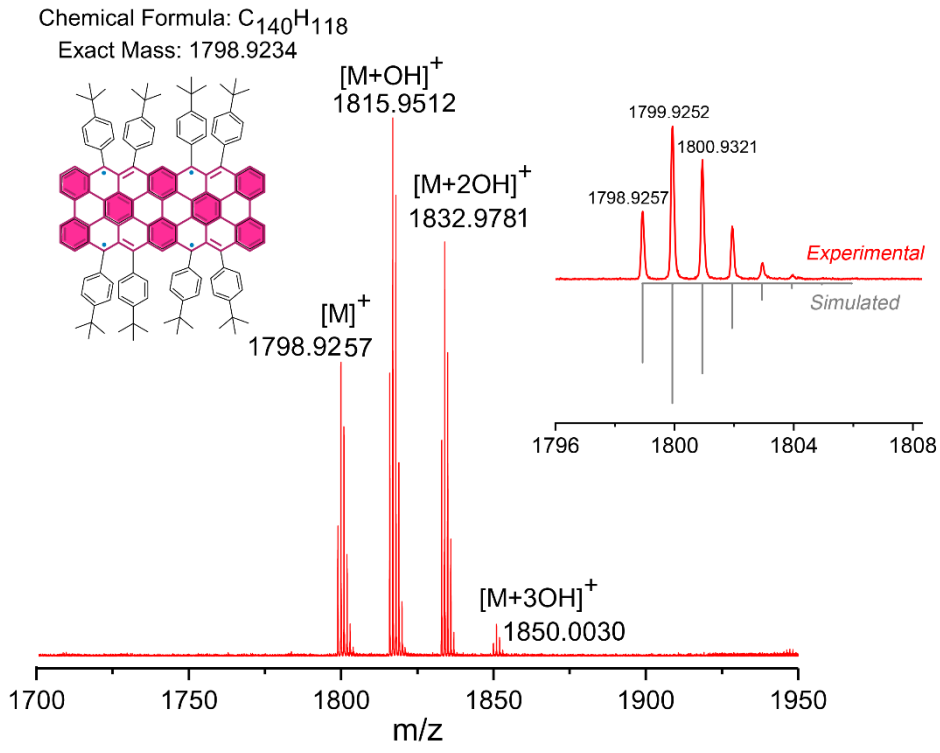

Figure S12: HR MALDI-TOF spectrum of **7-PA** in dithranol. The signals at m/z = 1815.9512, 1832.9781, and 1850.0030 were attributed to $[M+OH]^+$, $[M+2OH]^+$, and $[M+3OH]^+$, respectively, which could be generated from the instant reaction of **7-PA** with moisture and air during the measurement.

7. NMR spectra of new compounds

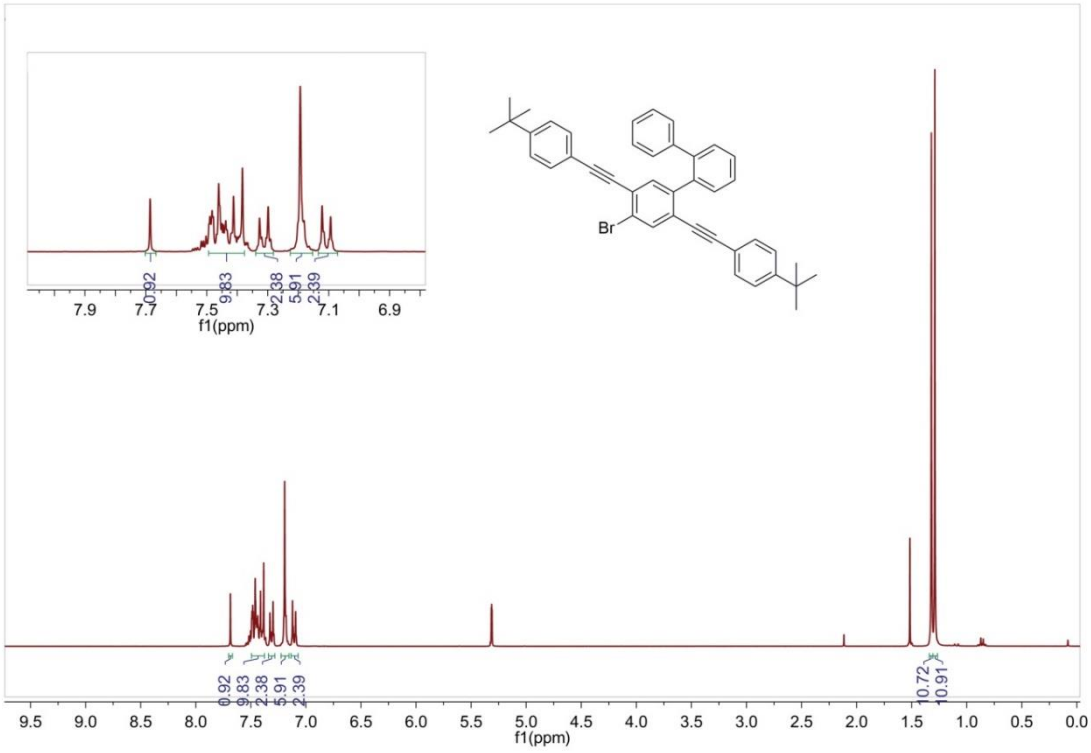

Figure S13: 300 MHz ^{1}H NMR spectrum of compound **8** in CD_2Cl_2 at RT.

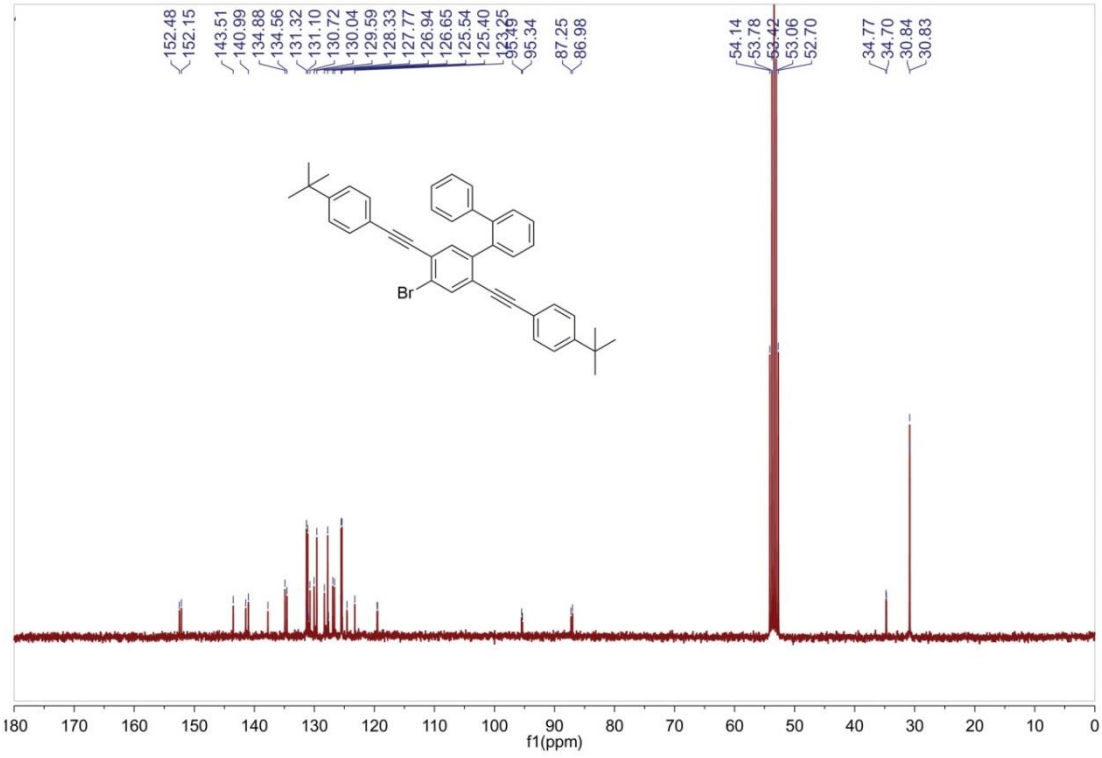

Figure S14: 75 MHz ^{13}C NMR spectrum of compound **8** in CD_2Cl_2 at RT.

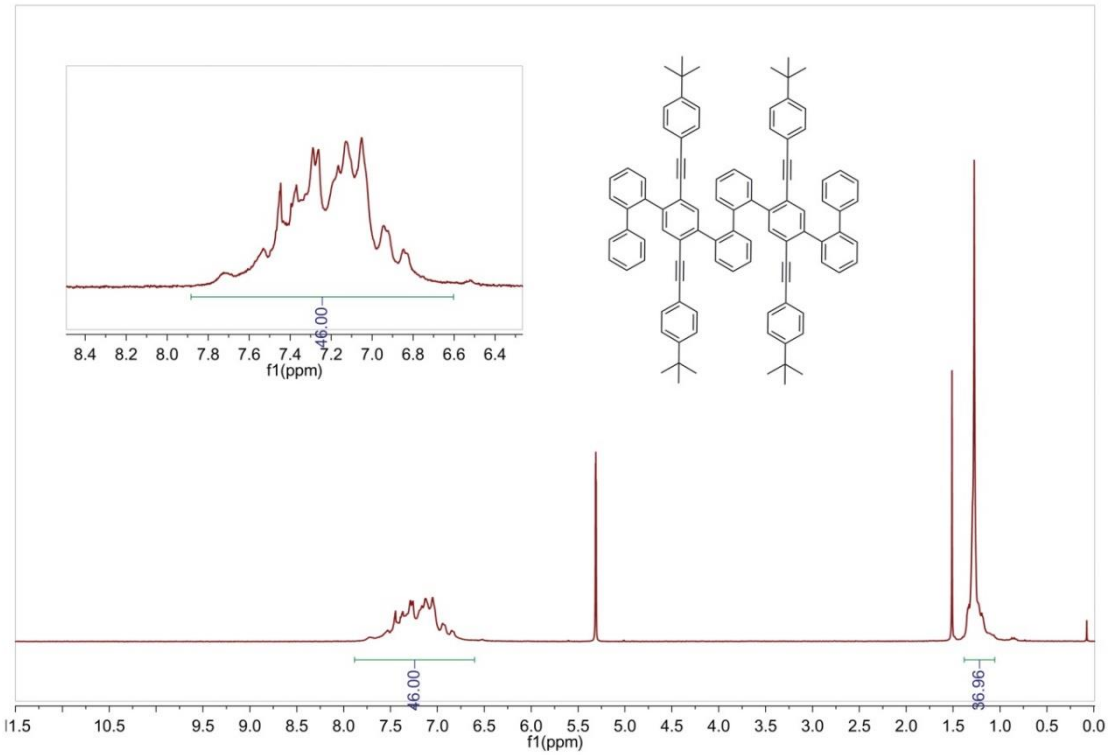

Figure S15: 300 MHz ^{1}H NMR spectrum of compound **1** in CD_2Cl_2 at RT.

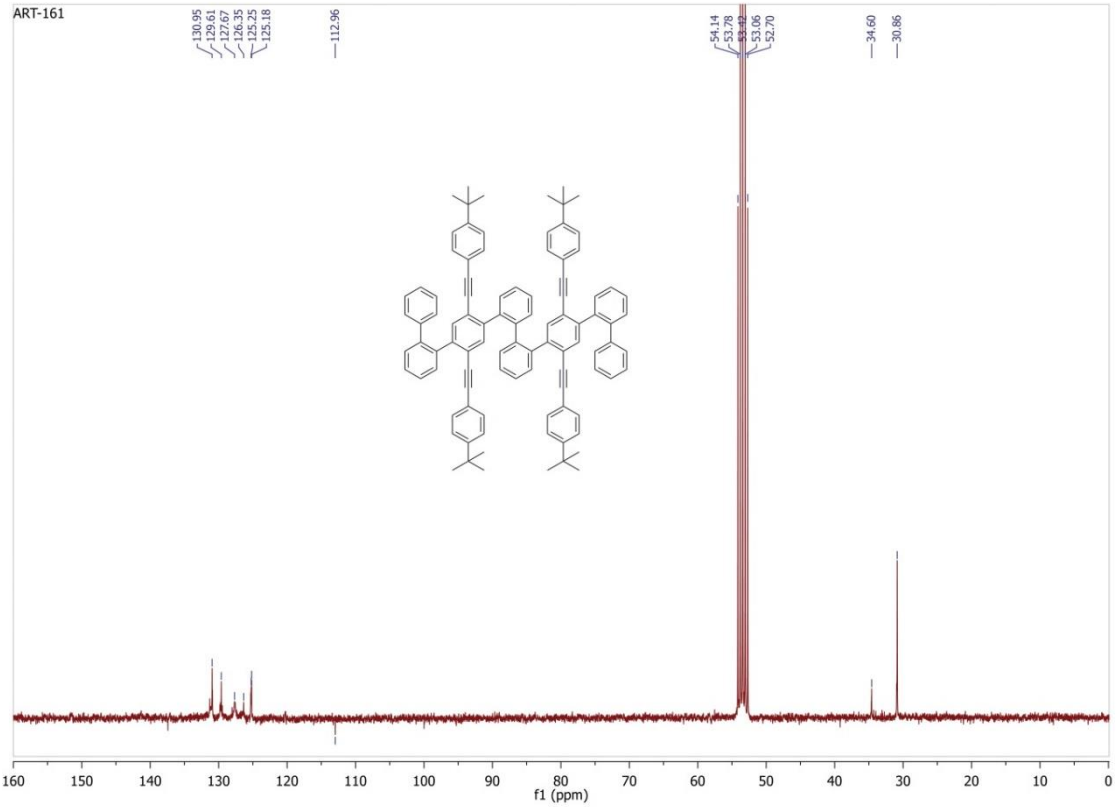

Figure S16: 75 MHz ^{13}C NMR spectrum of compound **1** in CD_2Cl_2 at RT.

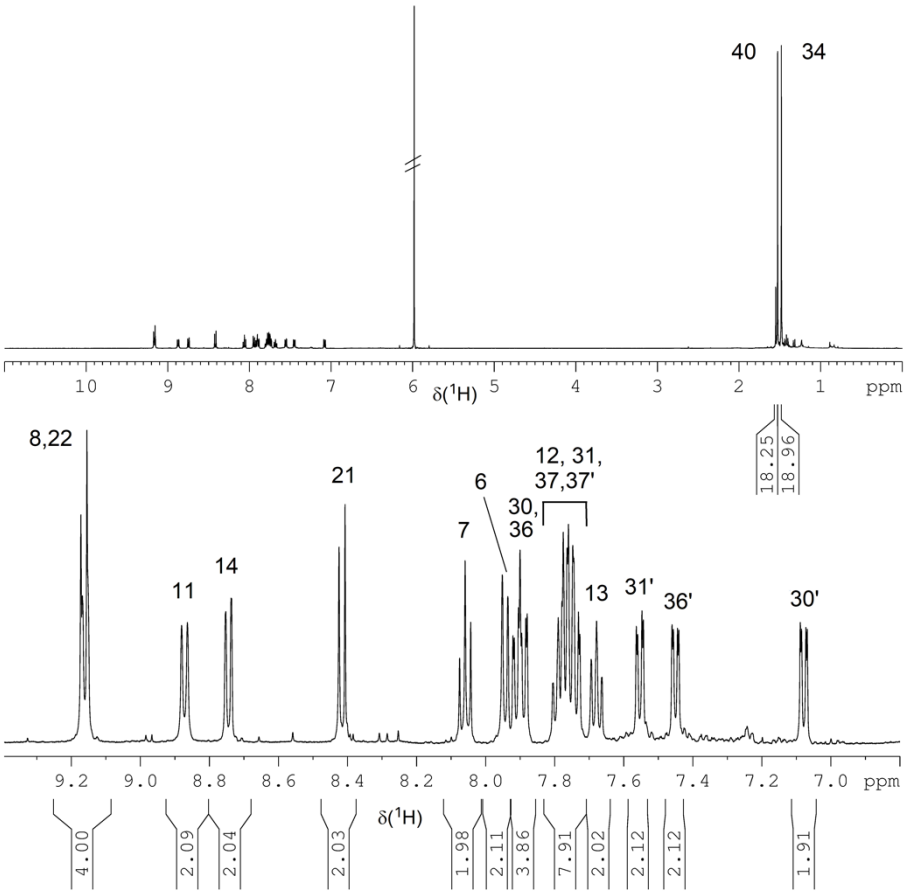

Figure S17: ^{1}H NMR spectrum (overview and region) of compound **2** ($C_2D_2Cl_4$, 30°C).

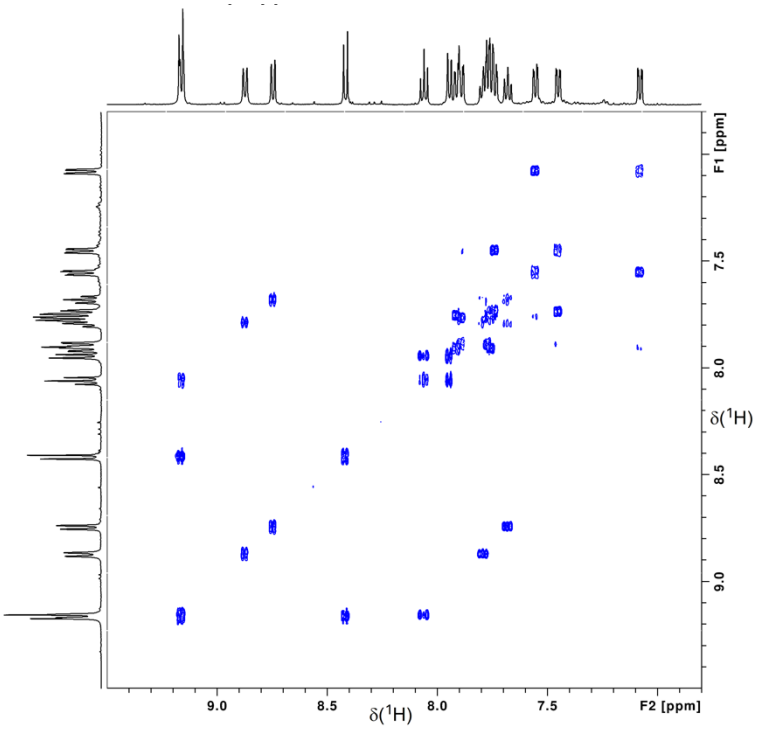

Figure S18: ^{1}H COSY spectrum (region) of compound **2** ($C_2D_2Cl_4$, 30°C).

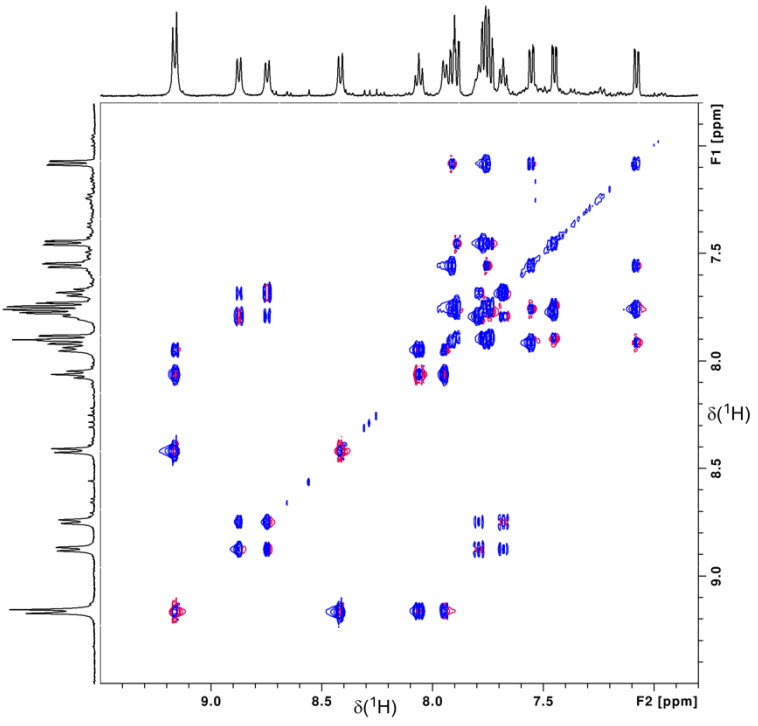

Figure S19: ^{1}H TOCSY spectrum (region) of compound **2** ($C_2D_2Cl_4$, 30°C).

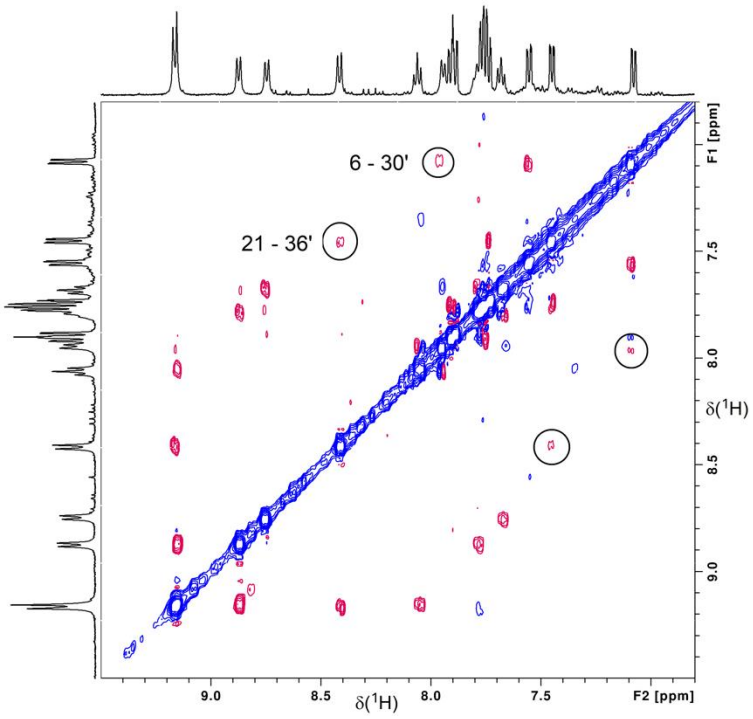

Figure S20: ^{1}H ROESY spectrum (region) of compound **2** ($C_2D_2Cl_4$, 30°C).

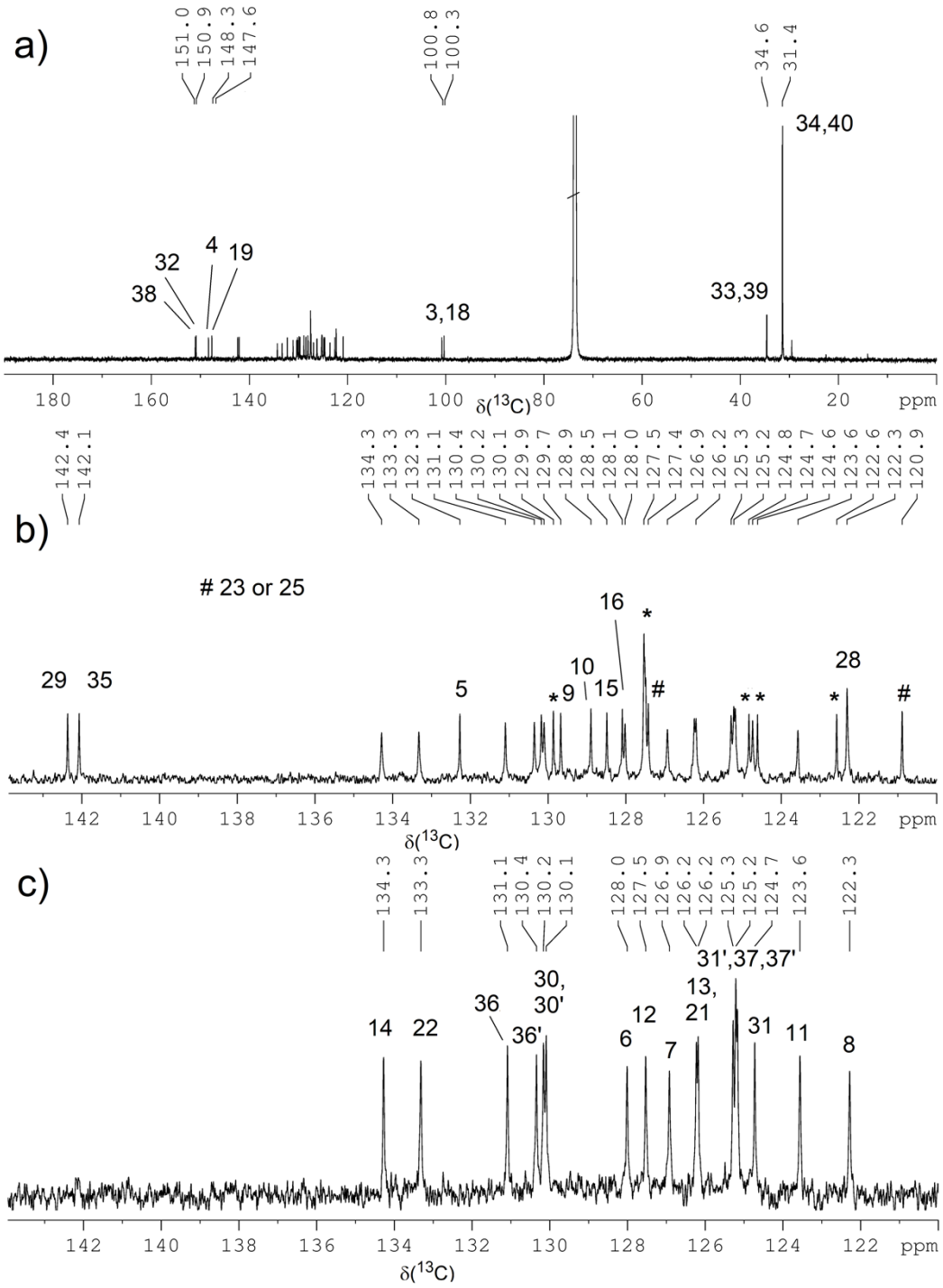

Figure S21: ^{13}C NMR spectra of compound **2**; overview (a) and enlarged region of aromatic carbon signals (b) with assignment of quaternary carbons. (c) depicts the DEPT135 spectrum (region) with assignment of aromatic CH carbons ($C_2D_2Cl_4$, 30°C). Signals marked with * could not be assigned.

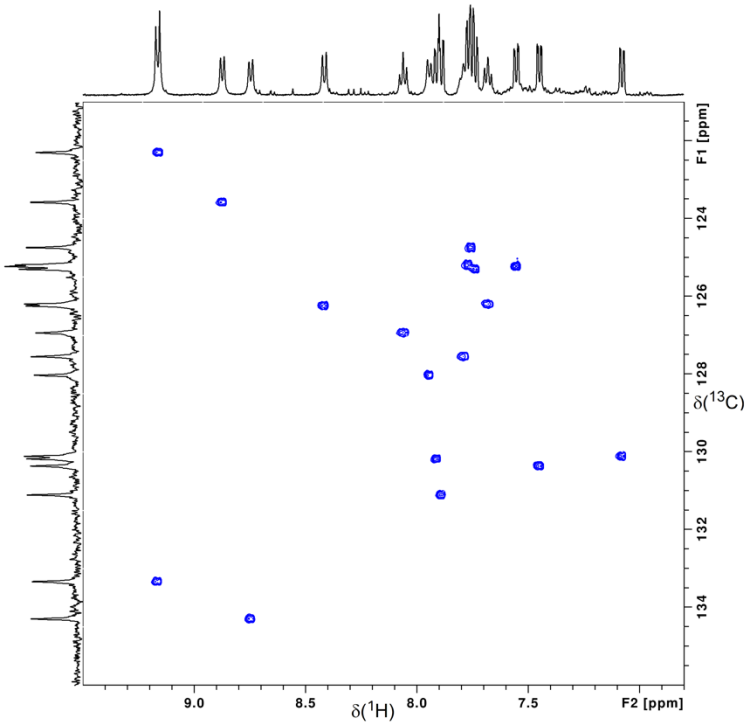

Figure S22: HSQC spectrum (region) of compound **2** ($C_2D_2Cl_4$, 30°C).

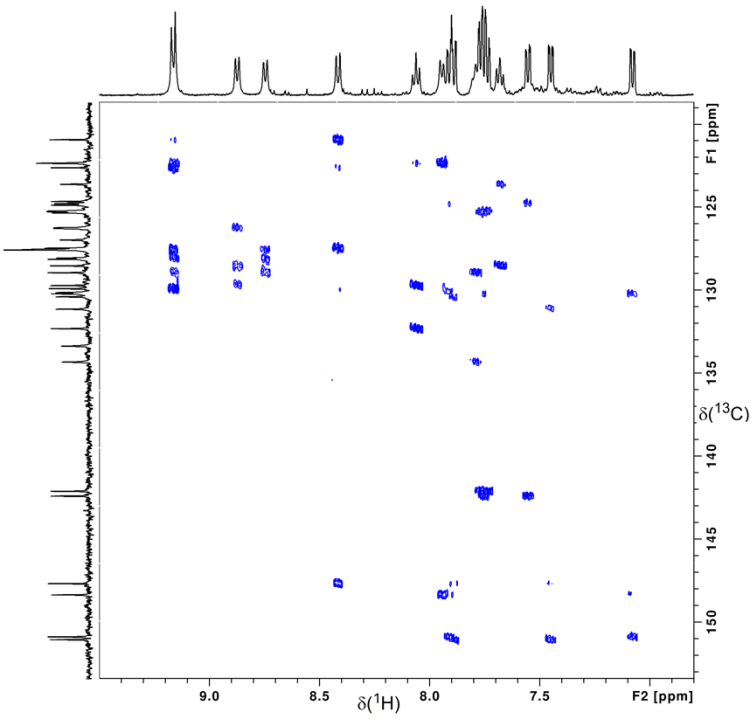

Figure S23: HMBC spectrum (region) of compound **2** ($C_2D_2Cl_4$, 30°C).

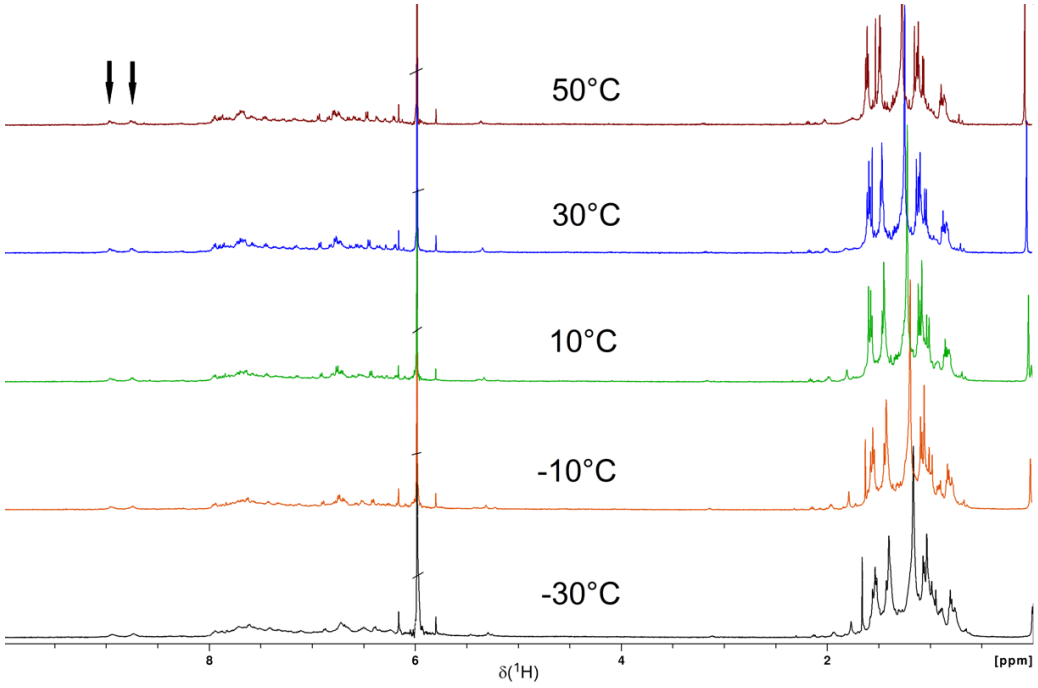

Figure S24: ^{1}H NMR spectra of **3** at different temperatures (solvent: $C_2D_2Cl_4$). The arrows indicate the signals of the protons in armchair arrangement [10]. The complexity of the spectrum of **2** is due to the presence of different stereoisomers resulting from the four chiral methine groups.

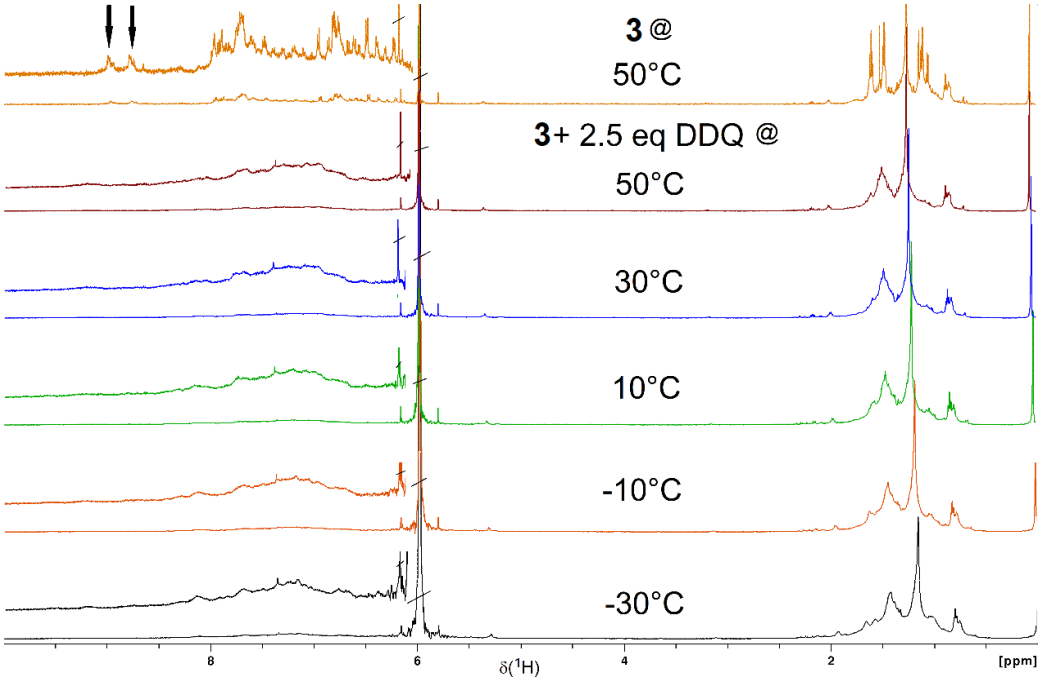

Figure S25: ^{1}H NMR spectra of **2** at 50°C (top) and of the same sample after addition of 2.5 equivalents of DDQ at different temperatures (solvent: $C_2D_2Cl_4$). The signals of the protons in armchair arrangement (arrows) and most probably also the other signals of protons of the *peri*-heptacene core of **7-PA** are extremely broadened. A signal broadening is also observed for the signals of the attached 4-*tert*. butyl phenyl groups but as expected to a lower extent.

8. References

[1] (a) Arslan, H.; Uribe-Romo, F. J.; Smith B. J.; Dichtel, W. R. *Chem. Sci.* **2013**, *4*, 3973-3978; (b) Ijpeij, E. G.; Beijer, F. H.; Arts, H. J.; Newton, C.; de Vries, J. G.; Gruter, G.-J. M. *J. Org. Chem.* **2002**, *67*, 169-176.

[2] T. Yanai, D. P. Tew, N. C. Handy, *Chem. Phys. Lett.* **2004**, *393*, 51-57.

[3] R. Krishnan, J. S. Binkley, R. Seeger, J. A. Pople, *J. Chem. Phys*. **1980**, *72*, 650

[4] Gaussian 09, Revision D.01, Frisch, M. J.; Trucks, G. W.; Schlegel, H. B.; Scuseria, G. E.; Robb, M. A.; Cheeseman, J. R.; Scalmani, G.; Barone, V.; Mennucci, B.; Petersson, G. A.; Nakatsuji, H.; Caricato, M.; Li, X.; Hratchian, H. P.; Izmaylov, A. F.; Bloino, J.; Zheng, G.; Sonnenberg, J. L.; Hada, M.; Ehara, M.; Toyota, K.; Fukuda, R.; Hasegawa, J.; Ishida, M.; Nakajima, T.; Honda, Y.; Kitao, O.; Nakai, H.; Vreven, T.; Montgomery, Jr., J. A.; Peralta, J. E.; Ogliaro, F.; Bearpark, M.; Heyd, J. J.; Brothers, E.; Kudin, K. N.; Staroverov, V. N.; Kobayashi, R.; Normand, J.; Raghavachari, K.; Rendell, A.; Burant, J. C.; Iyengar, S. S.; Tomasi, J.; Cossi, M.;Rega, N.; Millam, N. J.; Klene, M.; Knox, J. E.; Cross, J. B.; Bakken, V.; Adamo, C.; Jaramillo, J.; Gomperts, R.; Stratmann, R. E.; Yazyev, O.; Austin, A. J.; Cammi, R.; Pomelli, C.; Ochterski, J. W.; Martin, R. L.; Morokuma, K.; Zakrzewski, V. G.; Voth, G. A.; Salvador, P.; Dannenberg, J. J.; Dapprich, S.; Daniels, A. D.; Farkas, Ö.; Foresman, J. B.; Ortiz, J. V.; Cioslowski, J.; Fox, D. J. Gaussian, Inc., Wallingford CT, **2009**.

[5] E. D. Donato, M. Tommasini, G. Fustella, L. Brambilla, C. Castiglioni, G. Zerbi, C. D. Simpson, K. Müllen, F. Negri, *Chem. Phy.* **2004**, *301*, 81-93.

[6] K. Yamaguchi, *Self-consistent field: theory and applications*. (Eds.: R. Carbó, M. Klobukowski), Elsevier, Amsterdam, **1990**, pp. 727–823; S. Yamanaka M. Okumura, M. Nakano, K. Yamaguchi, *J Mol Struct: THEOCHEM*, **1994**; 310: 205–218.

[7] Lu, T.; Chen, F. Multiwfn: A Multifunctional Wavefunction Analyzer. *J. Comput. Chem.* **2012**, *33*, 580−592.

[8] Baker, J.; Scheiner, A.; Andzelm, J. Spin contamination in density functional theory. *Chem. Phys. Lett.* **1993**, *216*, 380–388.

[9] Ess, D. H.; Johnson, E. R.; Hu, X.; Yang, W. Singlet-triplet energy gaps for diradicals from fractional-spin density-functional theory. *J. Phys. Chem. A* **2011**, *115*, 76–83.

[10] M. R. Ajayakumar, Y. Fu, J. Ma, F. Hennersdorf, H. Komber, J. J. Weigand, A. Alfonsov, A. A. Popov, R. Berger, J. Liu, K. Müllen, X. Feng, *J. Am. Chem. Soc.* **2018**, 140, 6240-6244.